# Investigation of fiber Bragg grating based mode-splitting resonant sensors

**Carlo Edoardo Campanella,[1] Lorenzo Mastronardi,[1] Francesco De Leonardis,[1] Pietro Malara,[2] Gianluca Gagliardi,[2] and Vittorio M. N. Passaro[1,*]**

[1]*Dipartimento di Ingegneria Elettrica e dell'Informazione, Politecnico di Bari, Via Edoardo Orabona n. 4, 70125 Bari, Italy*

[2]*Istituto Nazionale di Ottica, Consiglio Nazionale delle Ricerche, Pozzuoli Napoli Italy*

**vittorio.passaro@poliba.it*

**Abstract:** In this paper, we report on theoretical investigation of split mode resonant sensors based on fiber Bragg grating (FBG) ring resonators and π-shifted fiber Bragg grating (π-FBG) ring resonators. By using a π-shifted Bragg grating ring resonator (π-FBGRR) instead of a conventional fiber Bragg grating ring resonator (FBGRR), the symmetric and antisymmetric resonance branches (i.e., the eigen-modes of the perturbed system) show peculiar and very important features that can be exploited to improve the performance of the fiber optic spectroscopic sensors. In particular, the π-FBGRR symmetric resonance branch can be taylored to have a maximum splitting sensitivity to small environmental perturbations. This optimal condition has been found around the crossing points of the two asymmetric resonance branches, by properly choosing the physical parameters of the system. Then, high sensitivity splitting mode sensors are theoretically demonstrated showing, as an example, a strain sensitivity improvement of at least one order of magnitude over the state-of-the-art.



**OCIS codes:** (230.0230) Optical devices; (130.6010) Sensors; (230.4555) Coupled resonators.

## References and links

1. W. Liang, L. Yang, J. K. S. Poon, Y. Huang, K. J. Vahala, and A. Yariv, "Transmission characteristics of a Fabry-Perot etalon-microtoroid resonator coupled system," Opt. Lett. **31**(4), 510–512 (2006).
2. A. Watkins, J. Ward, Y. Wu, and S. N. Chormaic, "Single-input spherical microbubble resonator," Opt. Lett. **36**(11), 2113–2115 (2011).
3. A. B. Matsko, L. Maleki, A. A. Savchenkov, and V. S. Ilchenko, "EIT in resonator chains: similarities and differences with atomic media," Jet Propulsion Laboratory, California Institute of Technology, 4800 -Oak-Grove Drive, Pasadena, California 91109–8099 (2003).
4. S. N. Chormaic, Y. Wu, and J. M. Ward, "Whispering gallery mode resonators as tools for non-linear optics and optomechanics," Proc. SPIE **8236**, 82361K (2012).
5. C. Ciminelli, C. E. Campanella, F. Dell'Olio, and M. N. Armenise, "Fast light generation through velocity manipulation in two vertically-stacked ring resonators," Opt. Express **18**(3), 2973–2986 (2010).
6. J. Zhu, S. K. Ozdemir, Y. F. Xiao, L. Li, L. He, D. R. Chen, and L. Yang, "On-chip single nanoparticle detection and sizing by mode splitting in an ultrahigh-Q microresonator," Nat. Photonics **4**(1), 46–49 (2010).
7. M. Li, X. Wu, L. Liu, X. Fan, and L. Xu, "Self-Referencing Optofluidic Ring Resonator Sensor for Highly Sensitive Biomolecular Detection," Anal. Chem. **85**(19), 9328–9332 (2013).
8. C. E. Campanella, F. De Leonardis, and V. M. N. Passaro, "Performance of Bragg grating ring resonator as high sensitivity refractive index sensor," IEEE Fotonica AEIT Italian Conf. on Photonics Technol., 1–4, May 12th-14th, Naples, Italy (2014).
9. C. A. Ramos, F. Morichetti, A. O. Moñux, I. M. Fernández, M. J. Strain, and A. Melloni, "Dual-Mode Coupled-Resonator Integrated Optical Filters," IEEE Photon. Technol. Lett. **26**(9), 929–932 (2014).
10. C. E. Campanella, C. M. Campanella, F. De Leonardis, and V. M. N. Passaro, "A high efficiency label-free photonic biosensor based on vertically stacked ring resonators," Eur. Phys. J. Spec. Top. **223**, 1–13 (2014).
11. C. E. Campanella, A. Giorgini, S. Avino, P. Malara, R. Zullo, G. Gagliardi, and P. De Natale, "Localized strain sensing with fiber Bragg-grating ring cavities," Opt. Express **21**(24), 29435–29441 (2013).
12. A. Yariv, "Universal relations for coupling of optical power between microresonators and dielectric waveguides," Electron. Lett. **36**(4), 321–322 (2000).
13. T. Erdogan, "Fiber Grating Spectra," J. Lightwave Technol. **15**(8), 1277–1294 (1997).

#218848 - $15.00 USD Received 25 Jul 2014; revised 15 Sep 2014; accepted 17 Sep 2014; published 9 Oct 2014

14. J. M. Choi, R. K. Lee, and A. Yariv, "Ring fiber resonators based on fused-fiber grating add-drop filters:application to resonator coupling," Opt. Lett. **27**(18), 1598–1600 (2002).
15. S. L. Chuang, *Physics of Optoelectronic Devices* (Wiley-Interscience, 1995).
16. J. Ctyroky, I. Richter, and M. Sinor, "Dual resonance in a waveguide coupled ring micro-resonator," Opt. Quantum Electron. **38**(9–11), 781–797 (2006).
17. P. Wang, Q. Wang, G. Farrell, T. Freir, and J. Cassidy, "Investigation of Macrobending Losses of Standard Single Mode Fiber with Small Bend Radii," Microw. Opt. Technol. Lett. **49**(9), 2133–2138 (2007).
18. A. Figotin and I. Vitebskiy, "Gigantic transmission band-edge resonance in periodic stacks of anisotropic layers," Phys. Rev. E Stat. Nonlin. Soft Matter Phys. **72**(3), 036619 (2005).
19. A. Othonos, K. Kalli, and Kyriacos, *Fiber Bragg Gratings: Fundamentals and Applications in Telecommunications and Sensing* (Artech House, 1999).
20. W. Liang, Y. Huang, Y. Xu, R. K. Lee, and A. Yariv, "Highly sensitive fiber Bragg grating refractive index sensors," Appl. Phys. Lett. **86**(15), 151122 (2005).
21. H. Y. Choi, M. J. Kim, and B. H. Lee, "All-fiber Mach-Zehnder type interferometers formed in photonic crystal fiber," Opt. Express **15**(9), 5711–5720 (2007).
22. B. Dong, D. P. Zhou, and L. Wei, "Temperature insensitive all-fiber compact polarization-maintaining photonic crystal fiber based interferometer and its applications in fiber sensors," J. Lightwave Technol. **28**(7), 1011–1015 (2010).
23. K. K. Qureshi, Z. Y. Liu, H. Y. Tam, and M. F. Zia, "A strain sensor based on in-line fiber Mach–Zehnder interferometer in twin-core photonic crystal fiber," Opt. Commun. **309**(15), 68–70 (2013).
24. J. R. Zheng, P. Yan, Y. Yu, Z. Ou, J. Wang, X. Chen, and C. Du, "Temperature and index insensitive strain sensor based on a photonic crystal fiber in line Mach– Zehnder interferometer," Opt. Commun. **297**(15), 7–11 (2013).
25. X. Bai, D. Fan, S. Wang, S. Pu, and X. Zeng, "Strain Sensor Based on Fiber Ring Cavity Laser With Photonic Crystal Fiber In-Line Mach–Zehnder Interferometer," IEEE Photon. J. **6**(4), 6801608 (2014).

## 1. Introduction

Recently, the mode-splitting resonator configurations have gained an increasing attention due to their important spectral features showing physical effects like zero transmission [1], Fano-type transmission [2], electromagnetically-induced-transparency (EIT)-like transmission [3], electromagnetically-induced-absorption (EIA)-like transmission [4], fast and slow light effects [5] and many others. Although these effects result of great importance in the fundamental Physics for creating new analogies between Optics and atomic/molecular Physics, in the last few years many research groups are focusing on possibility of exploiting the advantages offered from these physical effects in sensing applications, with the aim of translating them into an improvement for real life. To this purpose, a mode-splitting resonant sensor, able to detect the presence of the nanoparticle (NP), has been proposed [6] for achieving a better sensor detection limit. In this case, the split spectral nature is associated with the scattering effect arising from the presence of an NP, responsible of excitation of the two coupled counter-propagating eigen-modes of the optical cavity. A different resonance splitting, a priori imposed by coupling two ring cavities, has also been exploited to obtain a self-referencing sensing scheme in order to investigate the response of an optofluidic ring resonator [7]. In [8] the physics of a mode-splitting RI sensor based on a SOI Bragg grating ring resonator, having a splitting magnitude equal to the PBG spectral extension and almost insensitive to the fabrication tolerances [9], has been reported. A mode-splitting biosensor, formed by two vertically stacked SOI micro-ring resonators interacting with a microfluidic ring channel, has been also analysed [10]. In this case the splitting variation, due to the change of the coupling conditions between the two rings, has been proposed in order to selectively sense the presence of any biological species. Recently, the operating principle of the splitting mode sensors has been also demonstrated for strain sensing applications. In fact, the theoretical explanation and experimental demonstration of a mode-splitting strain sensor formed by including a Fiber Bragg Grating (FBG) in a closed fiber loop has been carried out [11]. For not vanishing values of FBG reflectivity, a split-mode resonant structure can be observed, associated to the degeneracy removal of two counter-propagating modes. The magnitude of the mode splitting has been used to sense the localized strain applied to the resonator in the FBG region, in a cavity-enhanced measurement system almost immune to environmental perturbations. Thus, the exploitation of the mode-splitting sensor spectral

#218848 - $15.00 USD Received 25 Jul 2014; revised 15 Sep 2014; accepted 17 Sep 2014; published 9 Oct 2014

features (i.e., cavity enhanced resolution, low sensitivity to fabrication tolerances and to environmental perturbations, as well as implementation of self-referencing spectroscopic sensing schemes) becomes a natural consequence for improving the performance of the optical sensors. Although it is unanimously recognized the ability of the conventional Bragg grating based optical-fiber sensors to measure a lot of physical parameters (such as strain, force, pressure, displacement, temperature, humidity, electrical field, refractive index, rotation, position, vibrations, radiation dose and many others) very high resolutions, the advantages offered from the splitting mode sensors and their features still result an unexplored, but very promising, research field.

The purpose of this paper is to theoretically investigate the split mode resonant sensors based on fiber Bragg grating ring resonator and π-shifted fiber Bragg grating ring resonators. In Section II we describe the theoretical model of the two sensor configurations in order to compare the physical effects involved when the Bragg wavelength is changed due to any environmental perturbation (i.e., strain, force, pressure, displacement, temperature, humidity, electrical field). In Section III we report one example of these devices used as strain sensors, by comparing the performance of these two configurations (i.e. Bragg grating and π-shifted Bragg grating ring resonators) and properly framing them in the recent state-of-the-art of the strain sensors. Finally, Section IV summarizes the conclusions.

## 2. Splitting mode sensors based on Bragg grating ring resonators

The considered fiber optic split mode resonant sensing architectures consist on fiber ring cavities in which a conventional Fiber Bragg grating in Fig. 1(a) or a π-shifted Fiber Bragg grating in Fig. 1(b), are included.

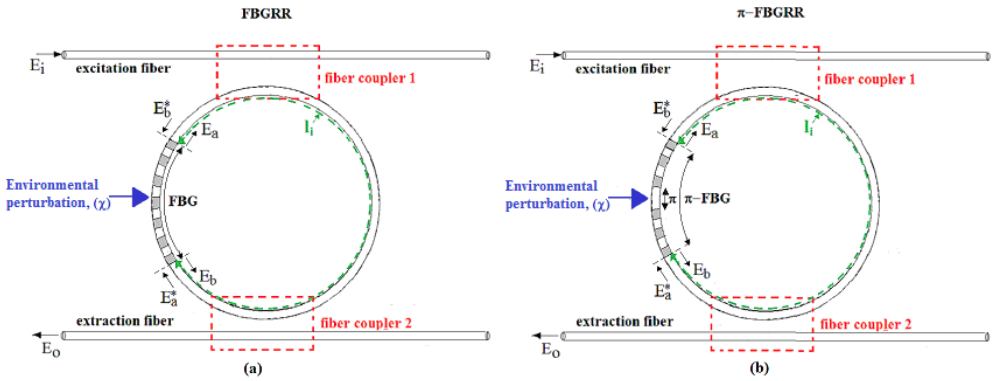


Fig. 1. Splitting mode resonant sensors, excited by an electric field $E_i$ introduced by the optical coupler 1. Their transmission response is evaluated at the fiber coupler 2. (a) Fiber Bragg Grating Ring Resonator (FBGRR), where an environmental perturbation (χ) is applied to the FBG; (b) π-shifted Fiber Bragg Grating Ring Resonator (π-FBGRR), where an environmental perturbation (χ) is applied to the π-FBG region.

It is known that the position of FBG or π-FBG inside the ring cavity does not affect the nature of the split resonant modes [6]. Thus, both FBGRR and π-FBGRR can be simply modelled by the transfer matrix, scattering matrix method and coupled mode theory [11]. We suppose the sensors as excited through fiber coupler 1, by a linearly polarized field $E_{in}$. In order to derive their spectral response (i.e., $T_{FBGRR}$ and $T_{\pi\text{-}FBGRR}$), the output optical field ($E_o$) has been evaluated at the end of the extraction fiber, belonging to the fiber coupler 2. Each coupler can be modelled by a transfer matrix [12] with negligible insertion loss, taking into account the fractions of the optical amplitudes transmitted ($\tau$) and coupled ($k$) via the evanescent coupler. Without any lack of generality, both fiber couplers are assumed with the same coupling coefficients. The π-FBG is physically composed by two identical FBGs,

#218848 - $15.00 USD Received 25 Jul 2014; revised 15 Sep 2014; accepted 17 Sep 2014; published 9 Oct 2014

separated by an optical path which introduces a phase delay $\Phi = \pi\lambda_B/(2\lambda)$ (with $\lambda_B$ the Bragg wavelength), for each counter-propagating wave generated inside the ring cavity. The FBGRR has been already modelled and experimentally proved in [11], where the environmental perturbation consisted in one localized strain applied to the FBG. About the π-FBGRR, if we consider as $E_a$, $E_b$* and $E_a$*, $E_b$ the amplitudes of the electric fields incoming and outgoing from the π-FBG [11,13], the π-FBG can be modelled via a product of transfer matrices:

$$\begin{bmatrix} E_a \\ E_b^* \end{bmatrix} = T_{FBG} \begin{bmatrix} e^{j\Phi} & 0 \\ 0 & e^{-j\Phi} \end{bmatrix} T_{FBG} \begin{bmatrix} E_a^* \\ E_b \end{bmatrix} = \begin{bmatrix} A_{11} & A_{12} \\ A_{21} & A_{22} \end{bmatrix} \begin{bmatrix} E_a^* \\ E_b \end{bmatrix} \tag{1}$$

where $T_{FBG}$ is the transfer matrix associated to the FBG, expressed as:

$$T_{FBG} = \begin{bmatrix} t - r^2/t & r/t \\ -r/t & 1/t \end{bmatrix} \tag{2}$$

with $t$ and $r$ the electrical field amplitudes transmitted and reflected from the FBG, respectively [15]:

$$\begin{aligned} t &= \frac{\Theta}{\Theta \cos h(\Theta \ell) + j\Delta\beta \sin h(\Theta \ell)} \\ r &= \frac{jK \sin h(\Theta L)}{\Theta \cos h(\Theta \ell) + j\Delta\beta \sin h(\Theta \ell)} \end{aligned} \tag{3}$$

with λ the length of each FBG. $\Theta, K$ and $\Delta\beta$ can be expressed as:

$$\Theta = \left[ |K|^2 - (\Delta\beta)^2 \right]^{\frac{1}{2}};\ K = \frac{\pi |\Delta n|}{\lambda_B};\ \Delta\beta = 2\pi n \left( \frac{\lambda_B - \lambda}{\lambda \lambda_B} \right); \tag{4}$$

where $n$ is the effective refractive index of the fiber, $|\Delta n|$ and $\lambda_B$ are the grating index contrast and the Bragg wavelength $\lambda_B = 2n\Lambda_B$, with $\Lambda_B$ the FBG period, respectively. Now, the following scattering matrix *Sc*, depending on the electrical field amplitudes transmitted ($t_{\pi FBG}$) and reflected ($r_{\pi FBG}$) from the π-FBG, can be written:

$$Sc = \frac{1}{A_{22}} \begin{bmatrix} \det(A) & -A_{21} \\ -A_{21} & \det(A) \end{bmatrix} = \begin{bmatrix} t_{\pi FBG} & r_{\pi FBG} \\ r_{\pi FBG} & t_{\pi FBG} \end{bmatrix} \tag{5}$$

Then, the spectral response of the π-FBGRR, $T_{\pi\text{-}FBGRR}$, can be derived by combining the scattering matrix formalism [11–16] with the elements of *Sc* matrix as:

$$T_{\pi - FBGRR} = \left| \frac{E_{out}}{E_{in}} \right|^2 = \left| \frac{1}{2} \left[ \frac{k^2 a e^{-j\beta l_i/2} \left( t_{\pi FBG} + r_{\pi FBG} \right)}{1 - \tau^2 a^2 e^{-j\beta l_i} \left( t_{\pi FBG} + r_{\pi FBG} \right)} + \frac{k^2 a e^{-j\beta l_i/2} \left( t_{\pi FBG} - r_{\pi FBG} \right)}{1 - \tau^2 a^2 e^{-j\beta l_i} \left( t_{\pi FBG} - r_{\pi FBG} \right)} \right] \right|^2 \tag{6}$$

where $l_i$ is the conventional fiber length, completing the resonant cavity together with the grating as in Fig. 1, and $a = \exp(-\alpha l_i/2)$ is the overall attenuation in a round trip due to the loss ($\alpha$) per unit length. The right hand side of Eq. (6) is a combination of the two "symmetric" and "antisymmetric" guided wave solutions [16]. Thus, the conventional FBGRR spectral response, $T_{FBGRR}$, can be easily derived by imposing $\Phi = 0$ from Eq. (6):

$$T_{FBGRR} = T_{\pi - FBGRR}\big|_{\Phi = 0} \tag{7}$$

#218848 - $15.00 USD Received 25 Jul 2014; revised 15 Sep 2014; accepted 17 Sep 2014; published 9 Oct 2014

In the spectral region where $t_{\pi FBG} \neq 1$, the combination of the symmetric (S) and antisymmetric (A) solutions of Eq. (6) is responsible of a spectral behavior characterized by a splitting mode structure. In this spectral range, the split modes are a consequence of the degeneration removal of the two counter-propagating resonant modes coupled via the FBG or π–FBG [11]. Otherwise, for $t_{\pi FBG} \approx 1$ the symmetric and antisymmetric solutions are quasi-degenerate. Differently from the conventional FBG, the π-FBG shows a resonant maximum in the transmission curve, centered at $\lambda_B$, where the π-FBGRR behaves in a quasi degenerate mode condition. With reference to Eq. (6), the symmetric resonant solutions, $\lambda_{RS}$, can be evaluated by considering those wavelengths for which the denominator of the S solution (i.e., $f_S$), given by:

$$f_S(\lambda) = 1 - \tau^2 a^2 e^{-j\frac{2\pi n}{\lambda} l_i} \left[ t_{\pi FBG}(\lambda) + r_{\pi FBG}(\lambda) \right] \tag{8}$$

vanishes, in order to satisfy the S dispersion equation:

$$e^{j\frac{2\pi n}{\lambda_{RS}} l_i} = \tau^2 a^2 \left[ t_{\pi FBG}(\lambda_{RS}) + r_{\pi FBG}(\lambda_{RS}) \right] e^{j2\pi q} \tag{9}$$

where $q$ is an integer (resonance order). Analogously, for the antisymmetric solution:

$$f_A(\lambda) = 1 - \tau^2 a^2 e^{-j\frac{2\pi n}{\lambda} l_i} \left[ t_{\pi FBG}(\lambda) - r_{\pi FBG}(\lambda) \right] \tag{10}$$

and the A dispersion equation is satisfied for $\lambda_{RA}$ as:

$$e^{j\frac{2\pi n}{\lambda_{RA}} l_i} = \tau^2 a^2 \left[ t_{\pi FBG}(\lambda_{RA}) - r_{\pi FBG}(\lambda_{RA}) \right] e^{j2\pi q} \tag{11}$$

The difference between the resonance wavelengths $\lambda_{RS}$ and $\lambda_{RA}$, evaluated for the same resonance order $q = q^*$, represents the splitting magnitude:

$$Split = \left| \lambda_{RS} - \lambda_{RA} \right|_{q=q^*} \tag{12}$$

If both Bragg gratings suffer of any environmental perturbation (χ), both the Bragg wavelengths will shift the spectral response of the device. In fact, the FBG and π-FBG spectral responses will suffer a Bragg wavelength shift ( $\Delta\lambda_B$ ) given by:

$$\Delta\lambda_B = 2n\Delta\Lambda + 2\Lambda\Delta n_g = \chi\lambda_B \tag{13}$$

where $\Delta\Lambda$ and $\Delta n_g$ are the period and the group index variation due to the perturbation, respectively. Indeed, the χ parameter takes into account how the Bragg wavelength shifts with respect to its initial value. Thus, due to the environmental perturbation (χ), being all the spectrum shifted of $\Delta\lambda_B$, both the S and A transcendental dispersion equations will be satisfied for the new resonance wavelengths, $\lambda_{RS}^{\chi}$ and $\lambda_{RA}^{\chi}$, as reported in Eq. (14) and (15) for π-FBG and FBG (i.e., π-FBG with $\Phi = 0$), respectively:

$$e^{j\frac{2\pi n}{\lambda_{RS}^{\chi}} l_i} = \tau^2 a^2 \left[ t_{\pi FBG}((1+\chi)\lambda_{RS}) + r_{\pi FBG}((1+\chi)\lambda_{RS}) \right] e^{j2\pi q^*} \tag{14}$$

$$e^{j\frac{2\pi n}{\lambda_{RA}^{\chi}} l_i} = \tau^2 a^2 \left[ t_{\pi FBG}((1+\chi)\lambda_{RA}) - r_{\pi FBG}((1+\chi)\lambda_{RA}) \right] e^{j2\pi q^*} \tag{15}$$

Thus, the new splitting magnitude related to χ (i.e. $Split^{\chi}$) will be:

#218848 - $15.00 USD Received 25 Jul 2014; revised 15 Sep 2014; accepted 17 Sep 2014; published 9 Oct 2014

$$Split^{\chi} = \left| \lambda_{RS}{}^{\chi} - \lambda_{RA}{}^{\chi} \right|_{q=q^*} \tag{16}$$

To describe the physical behavior of the device, we consider the parameters as reported in Table 1, whose assumed values are usual for fiber optics technology. In particular, the input and output fibers are conventional single mode fibers (SMF 28), while the π-FBGRR parameters are those usually used in manufacturing FBGs (i.e., $\lambda_B$ = 1.5605 μm with $|\Delta n|$ around $10^{-5}$). The overall length of the ring cavity has been chosen of the order of the tens of centimeters, (i.e., ring radii of the order of a few centimeters), which allows to neglect the bending loss associated to SMF 28 [17].

**Table 1. FBG physical parameters**

| Parameters | Assumed values |
|---|---|
| $n$ (SMF 28) | 1.457 |
| $\|\Delta n\|$ | $4 \times 10^{-5}$ |
| $\lambda_B$ | 1.5605 μm |
| $\Lambda_B$ | 535.5518 nm |
| $\ell$ | 2 cm |
| $\alpha_{loss}$ | $4.5 \times 10^{-6}$ m$^{-1}$ |
| $\tau$ | 0.975 |
| $k$ | $(1-\tau^2)^{1/2}$ |

By considering Eq. (7) with $l_i$ = 16 cm, we report in Fig. 2 the contour curve representing the transmission response (i.e., $T_{FBGRR}$) in the wavelength domain [1.560460 μm; 1.560620 μm] around $\lambda_B$, by assuming a fractional change of $\lambda_B$ (i.e., $\chi = \Delta\lambda_B / \lambda_B$) in the range [$-5 \times 10^{-6}$; $5 \times 10^{-6}$]. With the physical parameters reported in Table 1, the splitting mode spectral response can be clearly seen. In fact, for $\chi = 0$, the spectral behavior is characterized by split resonant modes, belonging to different resonance orders, with a splitting magnitude varying from a maximum value (in that spectral range belonging to the FBG reflection band and centered at $\lambda_B$) to a null value (i.e., at the band edge resonances of the FBG transmission curve where the reflectivity vanishes [18] and the degenerate mode condition occurs). The maximum value of the splitting magnitude is very close to the half free spectral range (FSR) of the conventional ring resonator (in the region of FBG maximum reflectivity), in analogy with the splitting-mode resonant system reported in [10]. The physical behavior of this device as a strain sensor has been explained and proved in [11] for a weak FBG (i.e., having a reflectivity $|r_{FBG}|^2$ = 15%), allowing to evaluate an analytical expression for the splitting magnitude as Eq. (16). As it is shown in Fig. 2, the degenerate mode conditions (i.e., the crossing points between the symmetric and antisymmetric resonance branches belonging to the same resonance order) occur at different wavelengths belonging to the spectral intervals associated to band edge resonances of the FBG transmission curve, depending on χ. The insets on the right report the open loop FBG spectral response associated to the contour curves for different values of χ (i.e., $\chi = 0$ for the black curve and $\chi = 2.5 \times 10^{-6}$ for the red curve). In the inset at the bottom of Fig. 2, a zoom of $T_{FBGRR}$ in the λ-range [1.560470 μm; 1.560480 μm] is sketched, when a positive χ in the range [$1 \times 10^{-6}$; $5 \times 10^{-6}$] is applied.

#218848 - $15.00 USD Received 25 Jul 2014; revised 15 Sep 2014; accepted 17 Sep 2014; published 9 Oct 2014

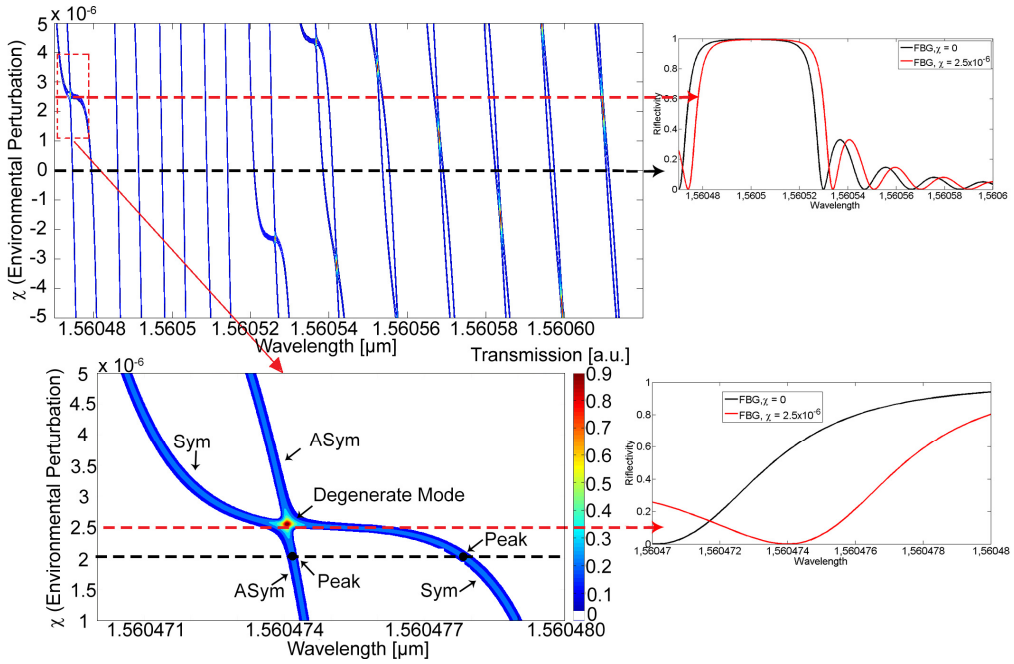


Fig. 2. FBGRR transmission $T_{FBGRR}$ contour curve in the λ-range [1.560470 μm; 1.560620 μm] evaluated with $l_i$ = 16 cm by changing χ from $-5 \times 10^{-5}$ to $5 \times 10^{-5}$ with a resolution of $5 \times 10^{-7}$; (Inset on the bottom) Zoom of $T_{FBGRR}$ in the λ-range [1.560470 μm; 1.560480 μm] being χ in the range [$1 \times 10^{-6}$; $5 \times 10^{-6}$]; the black dashed line refers to $\chi = 2 \times 10^{-6}$ for the two peak positions (black dots). (Insets on the right) FBG reflectivity in the same wavelength ranges.

Thus, ranging from $\chi = 1 \times 10^{-6}$ to $\chi = 5 \times 10^{-6}$ via the degenerate mode condition (fulfilled at λ = 1.560474 μm (first band edge transmission resonance of the open loop FBG transmission curve for $\chi = 2.5 \times 10^{-6}$), the spectral positions of symmetric (Sym) and antisymmetric (Asym) resonance branches are inverted in the spectrum. In other words, the crossing of the asymmetric resonance branches only occurs in a $\chi$ range centered at the bias value of $\chi = 2.5 \times 10^{-6}$. The different splitting magnitudes by passing for the crossing point depend on the achievable maximum reflectivity. Again, with reference to the inset of Fig. 2, the symmetric resonance branch has a sigmoidal shape, differently from the anti-symmetric one with linear shape. Due to these different shapes, they suffer of different shifts. In particular, the symmetric branch suffers of a wavelength shift of 8 pm (i.e., from 1.560471 μm to 1.560479 μm) for $\chi$ passing from $1 \times 10^{-6}$ to $4 \times 10^{-6}$. Differently, the anti-symmetric branch shift results one order of magnitude less than the symmetric one for the same Bragg wavelength shift. In Fig. 3 we report the transmission contour curve for a π-FBGRR as evaluated with the same physical and simulation conditions assumed in Fig. 2. The insets on the right report the open loop π-FBG spectral response associated to the contour curves for different values of $\chi$ (i.e., $\chi = 0$ for the black curve and $\chi = 1.833 \times 10^{-6}$ for the red curve). The inset on the bottom shows the zoom of $T_{\pi\text{-}FBGRR}$ in the λ-range [1.560496 μm; 1.560506 μm], where the degenerate mode condition is fulfilled. This occurs near the spectral region where the π-FBG shows its resonant maximum in the transmission curve, centered at $\lambda_B$, differently from the band edge transmission resonances of the conventional FBG transmission curve. As in Fig. 2, there is not only a different shape between Sym and Asym, implying for them a different wavelength shift due to $\chi$, but also an inversion between them by passing through the degenerate mode condition (i.e. centred at 1.560503 μm with a bias of $\chi$, implying $\Delta\lambda_B$ = 3 pm). As it can be deduced from the inset at the bottom, the Asym branch still remains locked to the Bragg wavelength.

#218848 - $15.00 USD Received 25 Jul 2014; revised 15 Sep 2014; accepted 17 Sep 2014; published 9 Oct 2014

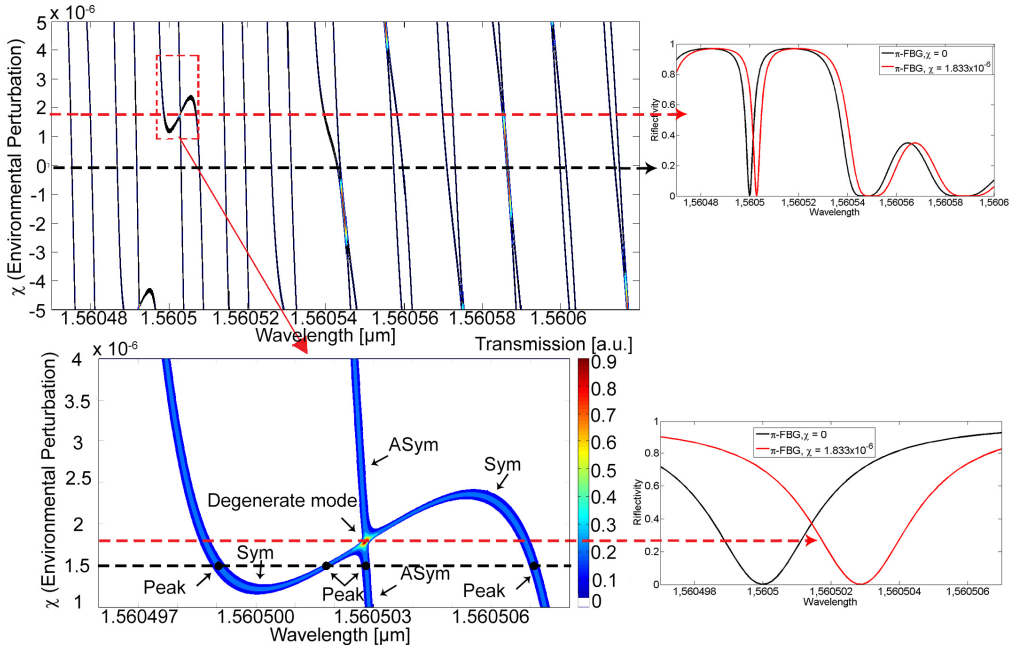


Fig. 3. π-FBGRR transmission ($T_{\pi\text{-}FBGRR}$) contour curve in the λ-range [1.560470 μm; 1.560620 μm] evaluated with $l_i$ = 16 cm by changing $\chi$ from $-5 \times 10^{-5}$ to $5 \times 10^{-5}$ with a resolution of $5 \times 10^{-7}$; (Inset on the bottom) Zoom of $T_{\pi\text{-}FBGRR}$ in the λ-range [1.560496 μm; 1.560508 μm] with χ in the range [$1 \times 10^{-6}$; $4 \times 10^{-6}$]. The black dashed line refers to $\chi = 1.5 \times 10^{-6}$, giving the four peak positions (black dots). (Insets on the right) π-FBG reflectivity in the same wavelength ranges.

Otherwise, the curvature for the Sym branch is revolved by passing from the increasing slope of the π-FBG transmission resonance maximum to the decreasing slope. From the simulations result that, in order to observe this curvature inversion in the Sym branch, the double maximum splitting achievable (about 9 pm) needs to be larger than the transmission resonance FWHM of the π-FBG (i.e., FWHM $_{\pi\text{-FBG}}$ = 3.6 pm), as:

$$2 \cdot Split^{\chi}{}_{MAX} = 2 \cdot \left| \lambda_{RS}{}^{\chi} - \lambda_{RA}{}^{\chi} \right|_{MAX} \Big|_{q=q^*} > FWHM_{\pi-FBG} \tag{17}$$

In fact, differently from the previous system, in this case the symmetric mode changes the sign of its slope around 1.560500 μm and 1.560506 μm, which in turn causes the presence of four peaks at four different wavelengths instead of two, as seen in Fig. 2. We have also proved that this Sym branch curvature change depends on $l_i$, and, in particular, the Sym branch curvature shape can be modulated by varying $l_i$. For this purpose, by choosing an appropriate value of $l_i$, the shape of the Sym branch becomes flat around the degenerate mode condition. To obtain this curvature shape for a given FWHM $_{\pi\text{-FBG}}$, we have numerically solved Eq. (14) and (15) as a function of $\chi$ and $l_i$, in order to find the $l_i$ value for which the double maximum splitting achievable (i.e., $2\,Split^{\chi}{}_{MAX}$) is equal to FWHM $_{\pi\text{-FBG}}$. In other words, with the same parameters of Table 1, by imposing a $\chi = \chi^* = 5 \times 10^{-6}$ and solving the equation as a function of $l_i$:

$$2 \cdot Split^{\chi^*,li}{}_{MAX} = 2 \cdot \left| \lambda_{RS}{}^{\chi^*,li} - \lambda_{RA}{}^{\chi^*,li} \right|_{MAX} \Big|_{q=q^*} = FWHM_{\pi-FBG} \tag{18}$$

a value of $l_i$ = 28 cm is found for which the curvature shape of Sym resonance branch is flat. This flatness of the Sym resonance branch is responsible of a maximum variation of the

#218848 - $15.00 USD Received 25 Jul 2014; revised 15 Sep 2014; accepted 17 Sep 2014; published 9 Oct 2014

splitting for small χ around the degenerate mode condition. In Fig. 4 we report the contour plot referring to this condition, where the flatness of the Sym resonance branch is clear.

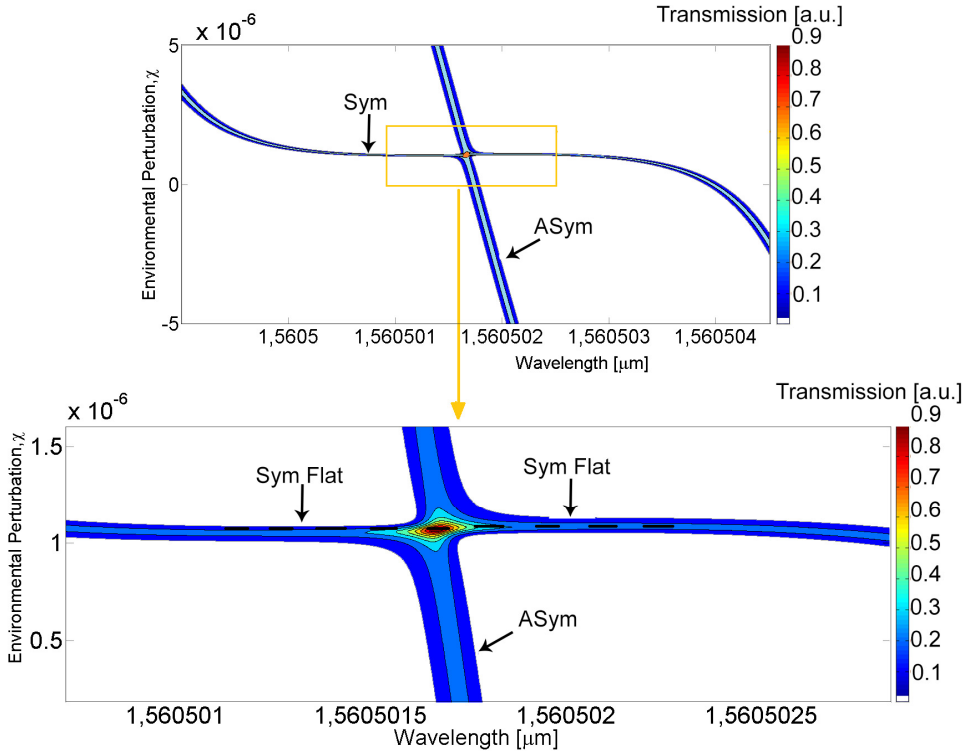


Fig. 4. π-FBGRR transmission ($T_{\pi\text{-}FBGRR}$) contour curve in the λ-range [1.560499 μm; 1.560504 μm] evaluated with $l_i$ = 28 cm for χ ranging from $-5 \times 10^{-6}$ to $5 \times 10^{-6}$ with a resolution of $5 \times 10^{-7}$. In the zoom (inset), the sym resonance branch is flat by imposing the condition of Eq. (18).

In Fig. 5, the $T_{\pi\text{-}FBGRR}$ contour curve is sketched in the wavelength domain [1.5604980 μm; 1.5605019 μm], by considering $l_i$ = 4.2 m and changing χ from $-5 \times 10^{-6}$ to $5 \times 10^{-6}$ with a resolution of $5 \times 10^{-7}$. The $l_i$ value has been assumed in order to include more resonance orders within the π-FBG maximum transmission band. In this case, it results:

$$2 \cdot Split^{\chi^*,li}{}_{MAX} = 2 \cdot \left| \lambda_{RS}{}^{\chi^*,li} - \lambda_{RA}{}^{\chi^*,li} \right|_{MAX} \Big|_{q=q^*} << FWHM_{\pi-FBG} \qquad (19)$$

In particular, without any applied $\chi$, the degenerate mode condition is fulfilled at $\lambda_B \approx 1.560500$ μm. Otherwise, this condition is red (blue)-shifted for positive (negative) values of χ. Thus, by passing from negative to positive values of $\chi$ via the degenerate mode condition (fulfilled for $\chi = 0$ at $\lambda_B = 1.550500$ μm), the spectral positions of the symmetric and anti-symmetric resonances are inverted in the spectrum. In this case, differently from the previous cases, by enlarging $l_i$ it is possible to remove the condition on the bias $\chi$ needed to obtain both the degenerate mode condition and only two peaks present for each resonance order included in the π-FBG transmission band. These described effects imply that the split-mode dynamics is strongly dependent from the length assumed by the conventional fiber $l_i$. Indeed, in this case the shape of the Sym resonance branch is not sigmoidal ($l_i$ = 16 cm) neither flat ($l_i$ = 28 cm), because Eq. (19) holds.

#218848 - $15.00 USD Received 25 Jul 2014; revised 15 Sep 2014; accepted 17 Sep 2014; published 9 Oct 2014

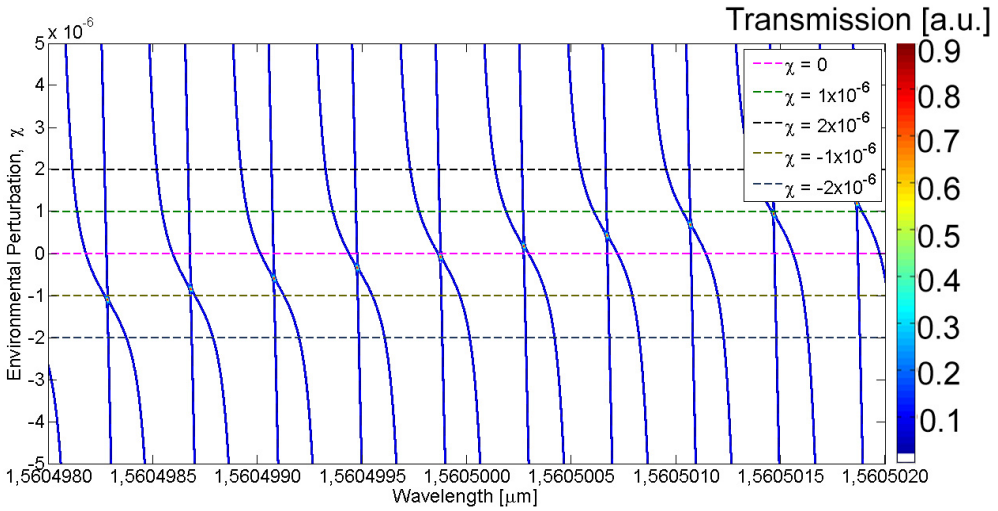


Fig. 5. $T_{\pi\text{-}FBGRR}$ in the λ-range [1.5604980 μm; 1.5605019 μm] with $l_i$ = 4.2 m. Contour curve by changing $\chi$ from $-5 \times 10^{-6}$ to $5 \times 10^{-6}$ with a resolution of $5 \times 10^{-7}$.

In other words, by comparing the dynamics of the asymmetric resonant branches obtained in Figs. 2–5, we can conclude how these are very strongly dependent from the physical parameters adopted to design the π-FBGRR. We summarize the obtained conditions in Fig. 6, where the revolved splitting dynamics (a), given by Eq. (17), the flat splitting dynamics (b) showing the maximum splitting sensitivity to $\chi$, as in Eq. (18), and the normal cross condition (d), as in Eq. (19), are reported.

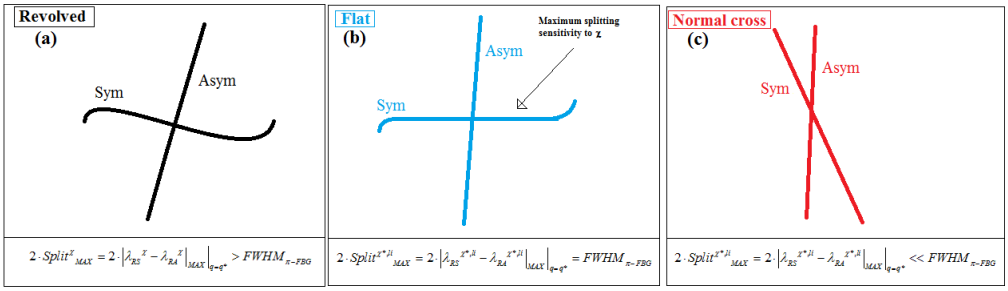


Fig. 6. Splitting dynamics of a π-FBGRR splitting mode sensor: (a) Revolved splitting dynamics given by Eq. (17); (b) Flat splitting dynamics as in Eq. (18); (c) Normal cross splitting dynamics of Eq. (19).

## 3. Performance evaluation of the splitting mode sensors

Once the physical behavior has been described in the previous section, here a comparison is presented in terms of performance of the two sensing systems of Fig. 1, if used as strain sensors. In particular, we suppose that SMF group index does not suffer from any variation, then $\Delta n_g = 0$ in Eq. (13) and, in turn, $\Delta\lambda_B = 2n\Delta\Lambda = \chi\lambda_B$ with $\chi = -0.79\varepsilon$, being $\delta\lambda_B / \delta\varepsilon = -0.79\lambda_B$ [11]. Indeed, in Fig. 7 we report the curve obtained by numerically solving Eq. (16), representing the splitting magnitude of FBGRR ($Split_{FBGRR}$, blue curve) due to an applied strain ranging from 2.57 με to 4 με, when $l_i$ = 16 cm. The starting point of 2.57 με depends on the strain bias ($\varepsilon_{bias}$) required to achieve the degenerate mode condition. This bias can be applied or by externally acting on the same sensor designed with the parameters reported in Table 1, or re-designing the FBG in order to achieve one new degenerate mode condition by imposing a new Bragg wavelength equal to $\lambda_B \cdot (1 - 0.79 \cdot \varepsilon_{bias})$, e.g. by designing $\Lambda_B = 0.5 \cdot \lambda_B \cdot (1-$

#218848 - $15.00 USD Received 25 Jul 2014; revised 15 Sep 2014; accepted 17 Sep 2014; published 9 Oct 2014

$0.79 \cdot \varepsilon_{bias})/n$. The same considerations are still valid for the π-FBG, in order to remove the $\varepsilon_{bias}$. The strain sensitivity $S_{FBGRR}$ (red curve) has a maximum value of 12.2 pm/με near the degenerate mode condition, while the maximum splitting achievable is around 2.4 pm. The splitting magnitude of π-FBGRR when $l_i$ = 16 cm has not been reported because the presence of the four peaks (see Fig. 3) is not suitable for a direct evaluation of the splitting magnitude. In Fig. 8 the splitting mode strain sensor performance is sketched when the double maximum splitting is equal to FWHM of π-FBG transmission resonance, according to Eq. (18), achievable only by using π-FBGRR. In fact, the π-FBGRR (solid) and FBGRR (dotted) curves of Fig. 8 are obtained by imposing $l_i$ = 28 cm when a strain ranging from 0 to 0.35 με is applied (still removing $\varepsilon_{bias}$). The π-FBGRR maximum splitting (solid blue curve) and the FBGRR one (dotted blue curve) are 1.8 pm (i.e., about $FWHM_{p\text{-}FBG}/2$) and 0.48 pm at 0.35 με, respectively. The π-FBGRR strain sensitivity near the degenerate mode condition can approach 22 pm/με (solid red curve), while it results only 2.2 pm/με for the FBGRR (see the dotted red curve). Thus, with these parameters the π-FBGRR shows a sensitivity enhancement factor of one order of magnitude with respect to FBGRR. For completness, referring to the condition expressed in Eq. (19), we evaluated for $l_i$ = 4.2 m the splitting magnitude of FBGRR and π-FBGRR due to an applied strain ranging from 0 to 5 με. In this case the π-FBGRR can have a sensitivity 1.8 times higher than FBGRR (0.1 pm/με versus 0.06 pm/με), far from the value for the optimal condition given by Eq. (18).

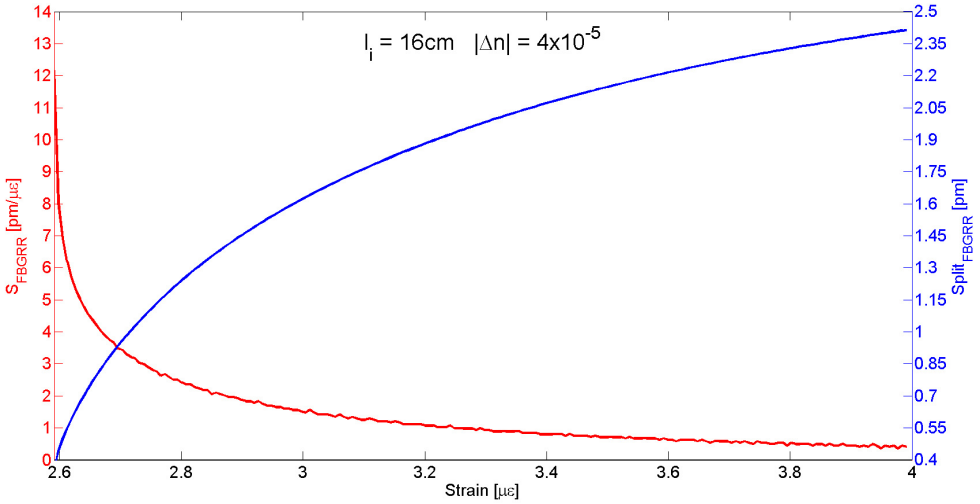


Fig. 7. Splitting magnitude of FBGRR ($Split_{FBGRR}$, blue curve) due to an applied strain ranging from 2.57 to 4 με when $l_i$ = 16 cm and $|\Delta n| = 4 \times 10^{-5}$. Strain sensitivity $S_{FBGRR}$ (red curve).

Moreover, we have also proved that by increasing (reducing) the index contrast |Δn| (i.e. by reducing (enlarging) the $FWHM_{\pi\text{-}FBG}$) to fulfil the optimal condition, the double maximum splitting (i.e., almost equal to the FSR) needs to be reduced (increased) and, in turn, $l_i$ increased (reduced). As an example for $|\Delta n| = 3 \times 10^{-5}$, Eq. (18) is satisfied for $l_i$ = 16 cm and $S_{\pi\text{-}FBGRR}$ results equal to 16.6 pm/με, while the splitting magnitude has a maximum splitting achievable of 1.6 pm at 3.8 με. On the other hand, for $|\Delta n| = 5 \times 10^{-5}$, Eq. (18) is fulfilled at $l_i$ = 45 cm, and $S_{\pi\text{-}FBGRR}$ = 7.2 pm/με while the maximum splitting achievable is 1.6 pm at 3.8 με. Thus, $S_{\pi\text{-}FBGRR}$ strictly depends on the structure parameters involved in fulfilling the condition of Eq. (18). Surely more complicated algorithmic procedures of parametric design should be able to further improve the maximum splitting sensitivity $S_{\pi\text{-}FBGRR}$ by selecting additional optimal conditions.

#218848 - $15.00 USD Received 25 Jul 2014; revised 15 Sep 2014; accepted 17 Sep 2014; published 9 Oct 2014

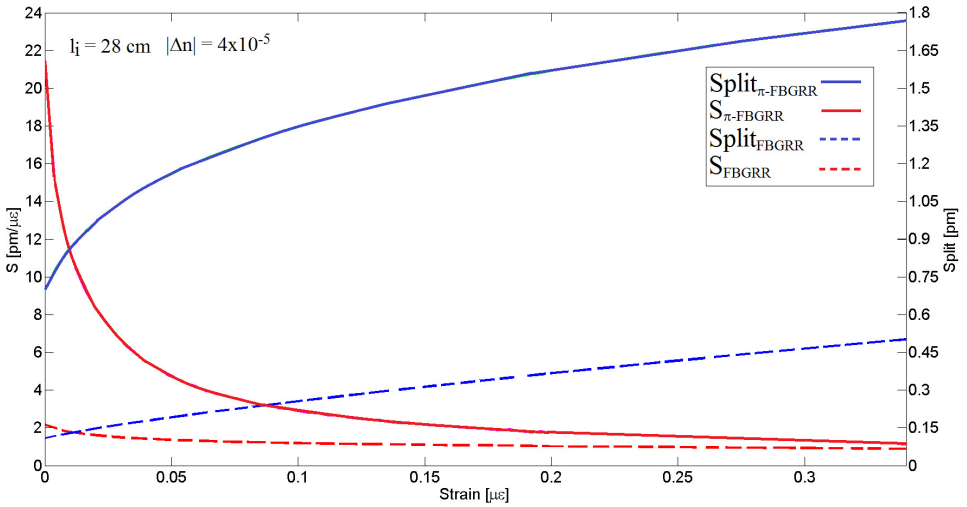


Fig. 8. Splitting magnitude of π-FBGRR ($Split_{\pi\text{-}FBGRR}$, solid blue curve) and FBGRR ($Split_{\pi\text{-}FBGRR}$, dashed blue curve) due to an applied strain ranging from 0 to 0.35 με when $l_i$ = 28 cm and $|\Delta n| = 4 \times 10^{-5}$ (optimal case). Strain sensitivity of π-FBGRR, $S_{\pi\text{-}FBGRR}$ (solid red curve), and FBGRR, $S_{FBGRR}$ (dashed red curve).

In addition, we have investigated the splitting and the sensitivity of the optimal case (i.e., $l_i$ = 28 cm) as a function of the coupling coefficient of the two fiber couplers. In fact, while in the previous optimal case of Fig. 8 a 5% power coupling coefficient (i.e., $1\text{-}\tau^2$, with $\tau = 0.975$) has been chosen, a performance comparison in terms of $Split_{\pi\text{-}FBGRR}$ is sketched in Fig. 9 by changing the power coupling coefficients from 2% ($\tau = 0.99$) to 3% ($\tau = 0.985$), 5% ($\tau = 0.975$), 7% ($\tau = 0.965$) and 10% ($\tau = 0.945$). As expected, the splitting magnitude $Split_{\pi\text{-}FBGRR}$ still remains almost the same, the maximum relative change being less than 3.6%. Further, $S_{\pi\text{-}FBGRR}$ has also revealed a very small dependence on coupling coefficients, less than 2%, in the whole strain range. This is consistent with the fact that, by reducing the coupling coefficients, it is possible to improve the resonator *Finesse* (i.e., the linewidths of the resonant split modes), so improving the sensor detection limit but not its sensitivity. About the losses, simulations confirm that it is possible to appreciate a not negligible variation of the linewidth of the split modes only if the system suffers of very large losses, at least of the order of 1 dB, much higher than those typically occurring in these fiber optic components.

In order to properly frame the obtained performance results in the context of the strain sensors, we have compared the splitting mode π-FBGRR sensitivity in the optimized condition (i.e., $l_i$ = 28 cm) with those recently achieved in literature [21–25]. A theoretical improvement factor of about one order or magnitude can be revealed with reference to the best strain sensitivity experimental values reported at the state-of-the-art [24,25]. The general considerations given in this paper still hold for any kind of environmental perturbation applied to these systems.

#218848 - $15.00 USD Received 25 Jul 2014; revised 15 Sep 2014; accepted 17 Sep 2014; published 9 Oct 2014

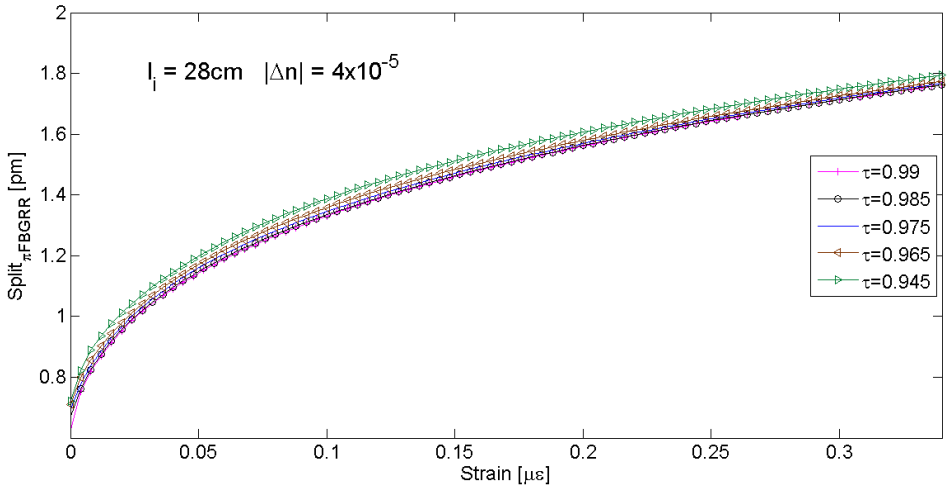


Fig. 9. Splitting magnitude ($Split_{\pi\text{-}FBGRR}$) of π-FBGRR versus the applied strain for power coupling coefficients of 2% (τ = 0.99), 3% (τ = 0.985), 5% (τ = 0.975), 7% (τ = 0.965) and 10% (τ = 0.945),when $l_i$ = 28 cm and $|\Delta n| = 4 \times 10^{-5}$ .

Indeed, if a temperature variation is considered as the environmental perturbation, the coefficient χ should become $C_T \Delta T$, with $C_T$ the temperature coefficient (i.e., depending on both thermal expansion coefficient and thermo-optic coefficient of the optical fiber) and $\Delta T$ the temperature variation [19]. As another example, with the same mechanism of transduction of the Bragg wavelength shift in splitting magnitude, RI sensors (i.e. $\Delta\Lambda = 0$ and, in turn, $\Delta\lambda_B = 2\Lambda\Delta n = \chi\lambda_B$) like those reported in [20] can be easily obtained by closing the FBG/π-FBG in a ring resonator, too. These sensors will have not only the conventional FBG and π-FBG characteristics, but also the mode-splitting sensor spectral features (i.e., cavity enhanced resolution, low sensitivity to fabrication tolerances and environmental perturbations, as well as easy implementation of self-referencing spectroscopic sensing schemes). Finally, it is worth noting that spectral interrogation of these split mode sensors is not a difficult task because it is sufficient to monitor the splitting variations of a single resonance. This can be done by injecting the cavity with a narrow-linewidth laser (that allows a resolution down to 0.1 pm) and continuously scanning its wavelength across the split resonance. At this point the amount of splitting can be measured directly from the cavity transmission [11], differently from the technique which involves the use of the optical spectrum analyzer and is limited by its resolution.

## 4. Conclusions

In this paper we investigate the split mode resonant sensors based on fiber Bragg grating ring resonators (FBGRR) and π-shifted fiber Bragg grating ring resonators (π–FBGRR). In these systems, the overall scattering effect, due to the presence of the fiber Bragg grating, creates two counter-propagating optical beams within the conventional fiber ring cavity, coupled via the grating effect. In the spectral response, this coupling gives rise to a split mode structure that is sensitive to a localized environmental perturbation applied to the FBG or π–FBG. To describe the physical behavior of the systems, we adopt a general model and consider the conventional physical parameters of the fiber optics technology. The eigen-modes of the systems, characterized by symmetric and anti-symmetric resonant branches, can cross each other in degenerate mode condition. The degenerate mode condition occurs in different spectral ranges (i.e., the first band edge resonance for FBGRR and the Bragg wavelength for π-FBGRR). For the π–FBGRR, by choosing particular physical conditions (i.e. the linewidth of the transmission maximum of the π–FBG equal to the double maximum splitting

#218848 - $15.00 USD Received 25 Jul 2014; revised 15 Sep 2014; accepted 17 Sep 2014; published 9 Oct 2014

achievable) it is possible to tailor the shape of the symmetric resonant branch in order to achieve a flat shape around the degenerate mode condition. This, in turn, creates a very high sensitivity of the π–FBGRR system to very small environmental perturbations. This improvement, although properly framed only in the context of the strain sensors, can be also referred to other kinds of splitting mode sensors, whose Bragg wavelength changes because of various environmental perturbations. Thus, with this mechanism of transduction of the Bragg wavelength shift in splitting magnitude, high sensitivity sensors showing together the FBG and π-FBG characteristics and the mode-splitting sensor spectral features (i.e., cavity enhanced resolution, low sensitivity to fabrication tolerances and to environmental perturbations, as well as implementation of self-referencing spectroscopic sensing schemes) can be easily obtained.

**Acknowledgments**

This work was supported by Politecnico di Bari under Fondo Ricerca di Ateneo (FRA) 2012 funding scheme.

#218848 - $15.00 USD Received 25 Jul 2014; revised 15 Sep 2014; accepted 17 Sep 2014; published 9 Oct 2014